PROCEEDINGS OF SCIENCE

Growths of Dark Matter Haloes and Galaxies in a ΛCDM Universe

Chung-Pei Ma[*†]
Department of Astronomy, 601 Campbell Hall, University of California, Berkeley, CA 94720, USA
E-mail: cpma@berkeley.edu

Numerical simulations are an indispensable tool for studying the late-time nonlinear evolution of cosmic structures, the theme of this workshop. The two Millennium simulations, each with 10 billion particles, have provided us with an unprecedentedly rich database to investigate and quantify the growths of dark matter haloes, the basic building blocks of the Universe. In this talk, I summarize recent results from the Millennium simulations for the merger rates and mass growth histories of dark matter haloes as a function of mass and redshift over a wide range of parameters: from 10^{10} to $10^{15} M_{\odot}$ for the descendant halo mass, 10^{-5} (minor mergers) to 1 (major mergers) for the progenitor mass ratio, and 0 to 15 for the redshift.

International Workshop on Cosmic Structure and Evolution - Cosmology2009,
September 23-25, 2009
Bielefeld, Germany

[*]Speaker.
[†]A footnote may follow.

PoS(Cosmology2009)012

In hierarchical cosmological models such as ΛCDM, host dark matter haloes of galaxies grow in mass and size primarily through mergers with other haloes. As the haloes merge, their more centrally concentrated baryonic components sink through dynamical friction and merge subsequently. Mergers are therefore responsible for the growth of stellar mass in galaxies, both directly via galaxy-galaxy mergers, and indirectly via the accretion of potentially star-forming gas. Furthermore, mergers help shape many important observational properties of galaxies, e.g., star formation rates, color and morphology transformations, dynamical states of stellar disks, and galaxy mass and luminosity functions. Having an accurate description of the mergers of dark matter haloes is therefore a key first step in quantifying the mergers of galaxies and in understanding the evolution of cosmic structure.

1. The Millennium Simulations

The Millennium [1] and Millennium-II [2] simulations are large N-body simulations of cosmological structure formation using the concordance ΛCDM cosmological parameters: $\Omega_m = 0.25$, $\Omega_b = 0.045$, $\Omega_\Lambda = 0.75$, $h = 0.73$, an initial power-law index $n = 1$ for the power spectrum of density fluctuations, and a normalization of $\sigma_8 = 0.9$. Unless otherwise specified, masses and lengths below are quoted in units of $\mathrm{M}_\odot$ and Mpc without the Hubble parameter h.

Both simulations follow the evolution of $2160^3 \approx 10^{10}$ particles from redshift 127 to redshift 0 using versions of the GADGET tree-PM code [3, 4]. The simulations differ in spatial scale and mass resolution: the Millennium Simulation uses a particle mass of $m_p = 1.18 \times 10^9\,\mathrm{M}_\odot$, a cubic box of side $L = 685\,\mathrm{Mpc}$, and a Plummer-equivalent force softening that is a factor of 10^5 smaller, $\varepsilon = 6.85\,\mathrm{kpc}$. The Millennium-II Simulation uses $L = 137\,\mathrm{Mpc}$ and $\varepsilon = 1.37\,\mathrm{kpc}$, both of which are a factor of 5 smaller than the values from the Millennium Simulation; the particle mass is therefore 125 times smaller, $m_p = 9.43 \times 10^6\,\mathrm{M}_\odot$. The two simulations have 60 outputs at identical redshifts between $z \approx 20$ and $z = 0$, spaced approximately equally in $\log z$, as well as additional snapshots (4 for the Millennium, 8 for the Millennium-II) at higher redshifts.

Subhalo merger trees are constructed in an identical fashion for the two simulations. Dark matter haloes are first identified at each snapshot using a Friends-of-Friends (FOF) group-finder with a linking length of 0.2 times the mean interparticle separation. All FOF groups with at least 20 particles are stored. The SUBFIND algorithm [5] is then applied to each FOF group to identify halo substructure. SUBFIND identifies local density maxima and performs an unbinding procedure to determine which particles in the FOF group are bound to each density peak. Substructures with at least 20 particles after unbinding are stored, resulting in a list of subhaloes associated with each FOF group in each simulation.

The main goal of our analysis presented in this talk is on quantifying the growth and mergers of FOF haloes. We therefore need merger trees of FOF haloes. The construction of merger trees of the FOF haloes from the subhalo trees in the public database is nontrivial due to halo fragmentations: subhaloes of a progenitor FOF halo may have descendants that reside in more than one FOF halo. Sometimes this is due to a physical unbinding event in which a subhalo formerly bound to an FOF is ejected out of the FOF system. Sometimes the fragmentation is spurious – a subhalo may oscillate in and out of the FOF group before finally settling in. Sometimes the FOF algorithm

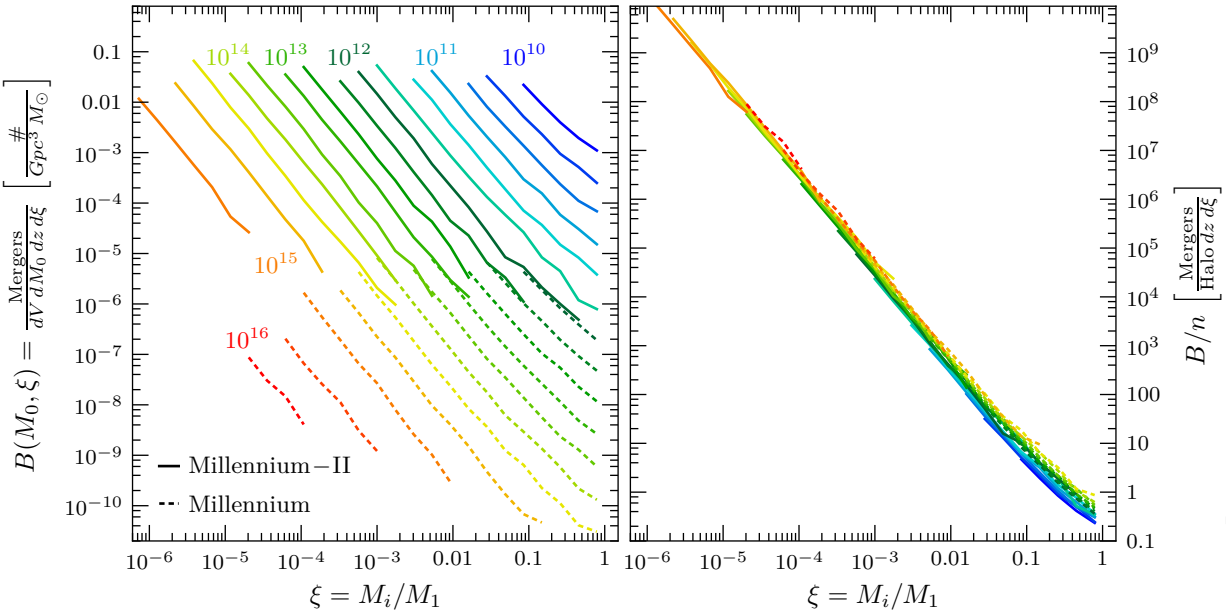

Figure 1: Left panel: The mean merger rate of $z = 0$ FOF haloes, $B(M_0, \xi)$, as a function of the mass ratio of the progenitors (ξ) and the descendant halo mass (M_0) over 6 orders of magnitude: 10^{10} to $10^{16} M_\odot$ from right (blue) to left (red). The Millennium-II results are shown in solid, while the results from the Millennium are in dashed curves. Right panel: The mean merger rate *per halo*, $B(M_0, \xi)/n(M_0)$. Normalizing $B(M_0, \xi)$ by the halo number density $n(M_0)$ collapses the curves in the left panel to nearly a single curve, indicating that B/n is nearly independent of M_0 and has a simple universal form. From Fig. 1 of [10].

incorrectly groups subhaloes that are unbound but only happen to pass by one another and should not be associated as a single FOF group.

Detailed comparisons can be found in [6, 8] for three types of algorithms for handling these fragmentation events. They are named "snip," "stitch," and "split," depending on whether the fragmented subhalo is ignored, stitched back to the original FOF halo in subsequent outputs, or split off from the FOF at earlier times. An assessment of the systematic differences in the merger rates derived from the algorithms is provided in the Appendix of [8]. The results presented below are computed using the "split-3" algorithm.

2. Halo Merger Rates

We have in hand a merger catalog once the merger trees of FOF haloes are constructed. Each catalog provides us with a list of descendant FOF haloes at redshift z_d with mass M_0, and for each descendant halo, its set of N_p FOF progenitors at $z_p = z_d + \Delta z$, where N_p can range from 1 (i.e. a single progenitor) to a large number, depending on the halo mass and the value of Δz. We label the rank-ordered progenitor mass with M_i, $i \in (1, 2, \ldots, N_p)$, and $M_1 \geq M_2 \geq \ldots M_{N_p}$. To ensure that only numerically resolved haloes are included in our study, we impose a minimum of 1000 particles for the descendant haloes and 40 particles for the progenitor haloes. For the Millennium Simulation, this criterion corresponds to a minimum halo mass of $1.2 \times 10^{12}\, \mathrm{M}_\odot$ for the descendant

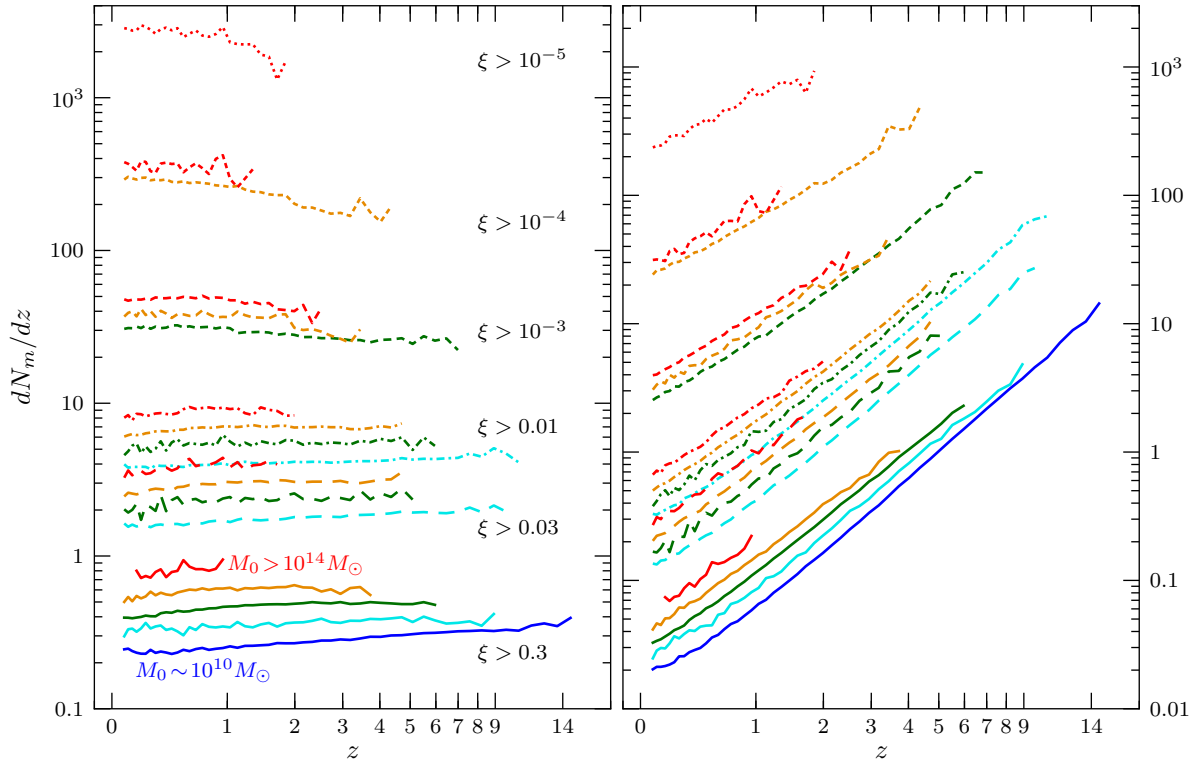

Figure 2: Time evolution of the mean halo merger rates *per halo* in units of per redshift, dN_m/dz (left panel), and in units of per Gyr, dN_m/dt (right panel) from the two Millennium simulations. The descendant mass M_0 and progenitor mass ratio ξ over five orders of magnitude are plotted. The weak dependence of the rates on M_0 is shown by the different colors: $\approx 10^{10}$ (blue), 10^{11} (cyan), 10^{12} (green), 10^{13} (orange). to $> 10^{14}\mathrm{M}_\odot$ (red). The line types denote different types of mergers, ranging from major mergers (solid) to extreme minor mergers (dotted) The rate dN_m/dz on the left is remarkably constant out to $z \sim 15$; the rapid rise of dN_m/dt with increasing z on the right is therefore largely due to the cosmological factor dt/dz, which spans a shorter time per unit z with increasing z. From Fig. 3 of [10].

and $4.7 \times 10^{10}\,\mathrm{M}_\odot$ for the progenitor. For Millennium-II, the minimum masses are $9.4 \times 10^{9}\,\mathrm{M}_\odot$ and $3.8 \times 10^{8}\,\mathrm{M}_\odot$ for the descendant and progenitor haloes.

We compute the merger rates at redshift z as a function of descendant mass M_0 and progenitor mass ratio $\xi = M_i/M_1$ (for $i > 1$). We define $B(M_0, \xi, z)$ to be the number of mergers per Mpc^3, dM_0, $d\xi$, and Δz with mass $M_0 \pm dM_0/2$ and mass ratio $\xi \pm d\xi/2$. The left panel of Fig. 1 shows the $z = 0$ results for $B(M_0, \xi, z = 0)$ as a function of progenitor mass ratio ξ from the two Millennium simulations (solid for Millennium II; dashed for Millennium). The colored curves correspond to different mass bins ranging from $10^{10}\,\mathrm{M}_\odot$ (blue) to $10^{16}\,\mathrm{M}_\odot$ (red).

The right panel of Fig. 1 shows the mean merger rate per halo, B/n, where each of the curves in the left panel has been divided by the number density of haloes in that mass bin. The collapse of the curves to nearly a single curve shows that the *per halo* merger rate B/n is nearly independent of halo mass. This nearly universal behavior was first reported in Fig. 6 of [6] for the Millennium Simulation alone. A comparison of the two figures helps illustrate the large dynamic range achieved when the two Millennium simulations are combined: the halo mass range has been increased by two

orders of magnitude here, and for each mass bin, the progenitor mass ratio is extended downward by also a factor of ~ 100, reaching $\xi \sim 10^{-6}$ for $M_0 = 10^{15}\,\mathrm{M}_\odot$.

The Millennium Simulation provided sufficient halo statistics for us to determine the halo merger rates up to $z \sim 6$ in our previous study. The higher mass resolution of the Millennium-II Simulation now allows us to probe redshifts up to ~ 15. The combined results from the two simulations are shown in Fig. 2, which plots the mean merger rate per unit redshift (left panel), dN_m/dz, and per unit time (right panel), dN_m/dt, as a function of redshift. These merger rates have been integrated over different ranges of $\xi \geq \xi_{\rm min}$, ranging from major mergers with $\xi_{\rm min} = 0.3$ (solid curves at bottom), to extreme minor mergers with $\xi_{\rm min} = 10^{-5}$ (dotted curve at top). Within each line type, the colors indicate different descendant mass bins ranging from 10^{10} (blue) to $> 10^{14}\mathrm{M}_\odot$ (red). Only the higher mass bins are plotted as $\xi_{\rm min}$ is lowered because minor mergers of low-mass haloes fall below the mass resolution limit.

We have explored simple algebraic expressions to fit the dimensionless mean merger rate B/n (in units of mergers per halo per unit redshift per unit ξ) from the combined Millennium dataset. An appealingly simple feature of the merger rates is that its dependence on the variables M_0, ξ, and z is approximately separable. We proposed in [10] this fitting form:

$$\frac{B}{n}(M,\xi,z) = A\left(\frac{M}{10^{12}M_\odot}\right)^\alpha \xi^\beta \exp\left[\left(\frac{\xi}{\tilde{\xi}}\right)^\gamma\right](1+z)^\eta\,, \tag{2.1}$$

where the best-fit parameters are $(\alpha,\beta,\gamma,\eta) = (0.133,-1.995,0.263,0.0993)$, $A = 0.0104$, and $\tilde{\xi} = 0.00972$. The near z-independence in the left panel of Fig. 2 is more striking than in our 2008 study due to the larger coverage in redshift here. In view of this lack of z-dependence, we choose to use the simpler factor of $(1+z)^\eta$ here rather than the growth rate of the density field employed in [6]. We note that the left panel of Fig. 2 does show mild variations in the redshift dependence among the different ξ bins: the rate increases slightly with increasing z for major mergers, while it declines somewhat for the very minor mergers ($\xi_{\rm min} \sim 10^{-4}$ to 10^{-5}). Since this variation is so minor and the minor merger regime is more prone to numerical resolution issues, we have opted for simplicity rather than a more complicated fitting form.

3. Environmental Dependence

The merger rates discussed above were determined as a function of the descendant mass, progenitor mass ratio, and redshift, regardless of where the haloes resided in the simulation box. The Millennium database is rich enough for us to quantify the merger rate as a function of a fourth variable, the halo environment.

We quantify a halo's local environment using the local mass density centred at the halo. We have tested three definitions of density. They are computed using the dark matter particles in a sphere of radius R centred at a halo, either with or without the central region carved out. Specifically, we define

$$\delta_R(\mathbf{x}) \equiv \frac{\rho_R(\mathbf{x}) - \bar{\rho}_m}{\bar{\rho}_m} \tag{3.1}$$

for a sphere of radius R, or

$$\delta_{R_o-R_i} \equiv \frac{\delta_{R_o}R_o^3 - \delta_{R_i}R_i^3}{R_o^3 - R_i^3} \tag{3.2}$$

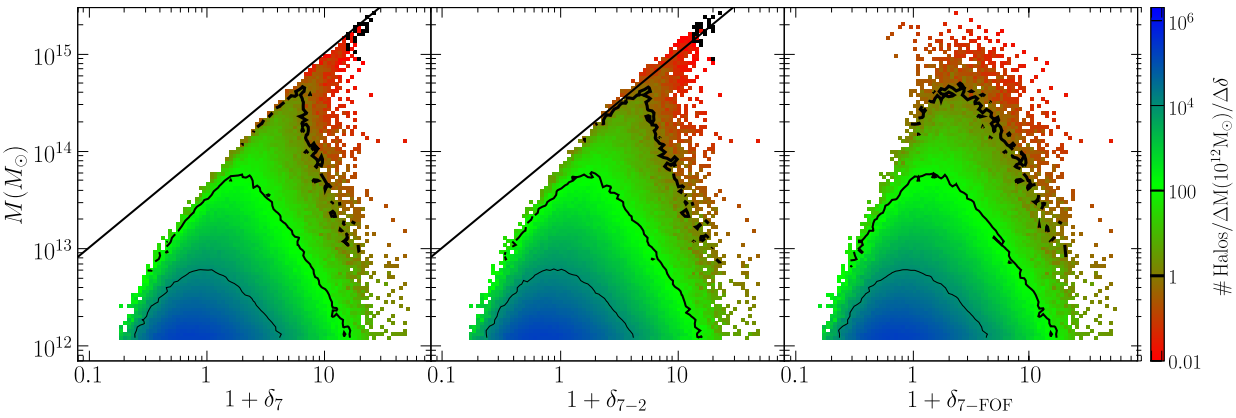

Figure 3: Scatter plots of halo mass vs three measures of halo environment for all FOF haloes above $1.2\times10^{12}M_\odot$ (1000 particles or more) in the $z=0$ Millennium Simulation output. The colour scale indicates the number of haloes present in each (δ,M) grid cell normalised by the bin size, and the contours are drawn at the 1, 100, and 10^4 bin levels (decreasing line width). The left panel uses $1+\delta_7$, the density in a sphere of radius $7h^{-1}$ Mpc centred at each halo. The black line is $1+\delta_7 = M/V_7/\bar{\rho}_m$ (see text). The middle panel shows $1+\delta_{7-2}$, the density in a shell between $2h^{-1}$ and $7h^{-1}$ Mpc. The right panel uses $1+\delta_{7-\mathrm{FOF}}$ by subtracting the halo mass from δ_7. At the high mass end, the halo itself is the main contribution to δ_7 and δ_{7-2}, leading to the tight correlation between δ and M in the upper right region in the left and middle panels. The right panels shows that this correlation is largely removed when $\delta_{7-\mathrm{FOF}}$ is used, which subtracts out the FOF mass of the central halo. The variable $\delta_{7-\mathrm{FOF}}$ is therefore a more independent measure of the immediate environment *outside* of the haloes. From Fig. 1 of [7]

for a shell of inner and outer radii R_i and R_o. Here $\bar{\rho}_m$ is the mean matter density in the simulation box, and $\rho_R(\mathbf{x})$ is the mean density of a sphere of radius R centred at $\mathbf{x}$. We also define an environmental measure, $\delta_{R-\mathrm{FOF}}$, computed by subtracting out the FOF mass M of the central halo within a sphere of radius R:

$$\delta_{R-\mathrm{FOF}} \equiv \delta_R - \frac{M}{V_R\bar{\rho}_m}, \tag{3.3}$$

where V_R is the volume of a sphere of radius R. Note that unlike the shell measure, this measure makes no assumption about the central halo's shape

Fig. 3 is a scatter plot of the mass of every FOF halo (above 1000 particles) at $z=0$ in the Millennium Simulation versus its local $1+\delta$. Three definitions of local density are shown for comparison: all mass within a $7h^{-1}$ Mpc sphere (δ_7; left panel), all mass within $7h^{-1}$ Mpc excluding the central $2h^{-1}$ Mpc (δ_{7-2}; middle panel), and all mass within $7h^{-1}$ Mpc excluding the central FOF mass ($\delta_{7-\mathrm{FOF}}$; right panel).

Fig. 3 shows that galaxy-size haloes ($\sim 10^{12}M_\odot$) reside in a wide range of environmental densities from extreme underdense regions of $\delta\sim-0.8$ to regions with $\delta>20$. The three panels show similar distributions of δ for these low mass haloes regardless of the definition of δ used. The high mass haloes, on the other hand, have very different distributions of δ. At $5\times10^{14}M_\odot$ and above, the spherical and shell measures of overdensity, δ_7 and δ_{7-2}, are seen to be tightly correlated with the halo mass (left and middle panels). In addition, all the points lie close to the line that represents the density in a $7h^{-1}$ Mpc sphere computed from the FOF halo mass *alone*, that is, $M/V_7/\bar{\rho}_m$, where V_7 is the volume of a sphere of radius $7h^{-1}$ Mpc. This trend clearly indicates

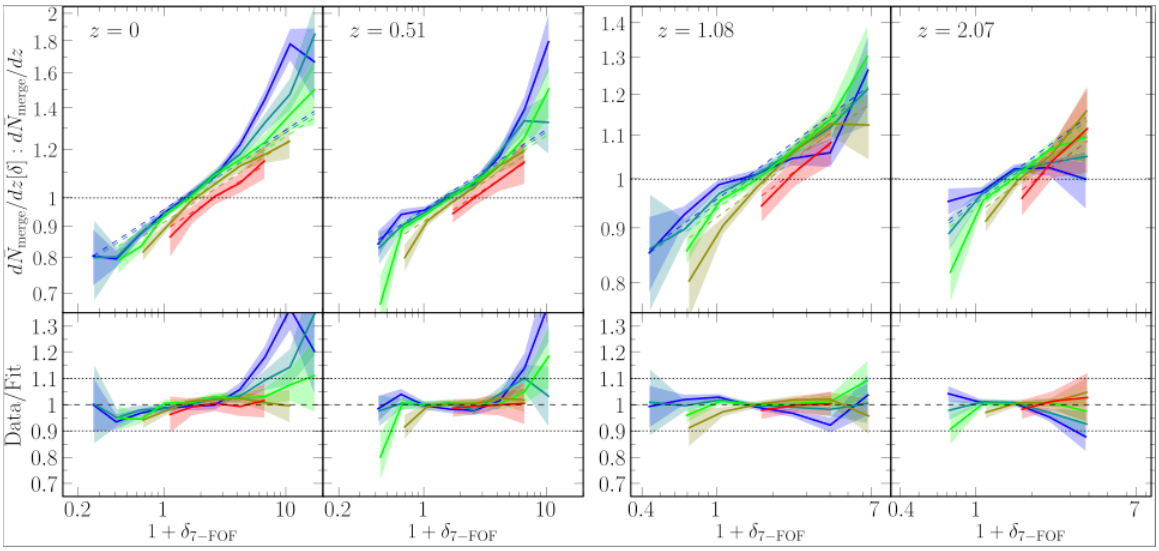

Figure 4: Dependence of the mean merger rate on the halo environment variable $1+\delta_{7-\rm FOF}$. Four redshifts $z \approx 0, 0.5, 1$ and 2 (left to right) are shown. Within each figure, the top panel shows the ratio of the mean merger rate for haloes in a given environment to the global mean merger rate. The bottom panel plots the ratio of the simulation results to the fits, showing that equations (3.4) and (3.5) are generally accurate to within 10% (indicated by the dotted horizontal line). The colours correspond to the five mass percentile bins (red for the highest and blue for the lowest mass bin); the bands correspond to Poisson errors. This figure shows that the positive correlation of the merger rate with environmental density is present at all mass and redshift ranges probed.

that the central haloes are dominating the local overdensity at masses above $\sim 5\times 10^{14} M_\odot$, and both δ_7 and δ_{7-2} are tracing the central halo mass rather than the overdensities in the neighbourhood *outside* the virial radius of the halo. Even though δ_{7-2} subtracts out the central $2h^{-1}$ Mpc regions, the tight residual correlation seen in the middle panel suggests that this quantity does not cleanly remove the contribution made by the central halo, probably because these massive haloes extend well beyond $2h^{-1}$ Mpc. The right panel of Fig. 3 shows that $\delta_{7-\rm FOF}$ of equation (3.3) is capable of disentangling the tight correlation between halo mass and density seen for δ_7 and δ_{7-2}; $\delta_{7-\rm FOF}$ is therefore a more robust measure of the environment *outside* of a halo's virial radius.

We find the environmental dependence of the merger rate to be well approximated by

$$\frac{dN_{\rm merge}}{dz}(\delta, M, z) \approx \frac{dN_{\rm merge}}{dz}(M,z) \times f(\delta, M)\,, \tag{3.4}$$

where

$$f(\delta_{7-\rm FOF}, M) = 0.963\,(1+\delta_{7-\rm FOF})^{0.130} \left(\frac{M}{10^{12} M_\odot}\right)^{-0.0156}\,, \tag{3.5}$$

and we have made use of the fact that the environmental dependence is independent of ξ to define f, and $dN/dz(M,z)$ is the global merger rate, which is related to B/n in equation (2.1) by integrating the latter over the relevant range of progenitor mass ratio ξ. The resulting fit is shown as dashed curves in the upper row in Fig. 4, and the ratio of the simulation data to the fits is shown in the lower rows. The fits are seen to be accurate to within 10% for a wide range of δ and M, except for low mass haloes with $\delta > 5$ at $z \approx 0$ and 0.5, where the rates steepen suddenly.

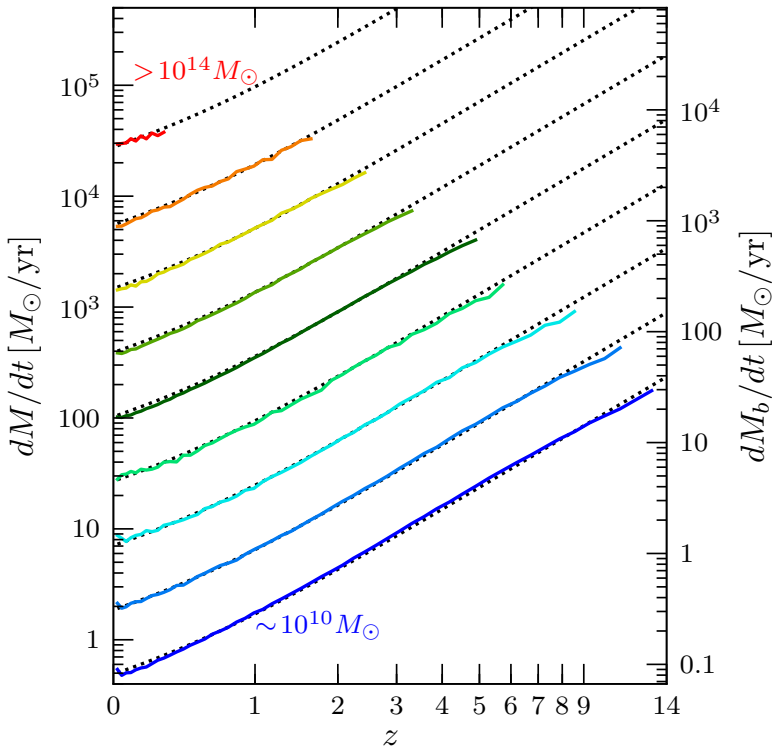

Figure 5: Mean mass accretion rate of dark matter onto haloes as a function of redshift from the two Millennium simulations (solid curves) for halo mass ranging from $10^{10}M_\odot$ to $>10^{14}M_\odot$. The dashed curves show the accurate fit provided by equation (4.1). The right-hand side of the vertical axis labels the mean accretion rate of baryons, M_b, assuming a cosmological baryon-to-dark matter ratio of 1/6. From Fig. 4 of [10].

4. Mass Accretion Rates

Thus far I have presented results for the instantaneous rates of halo mergers as a function of redshift, descendant mass, progenitor mass ratio, and halo environment. A related set of statistics that are important for quantifying halo growths is the mass growth history of individual haloes. These two quantities are clearly related since mergers are a primary process for haloes to gain mass. Mergers, however, are not the only process responsible for halo growth in N-body simulations; "diffuse" accretion of unresolved haloes or dark matter particles also makes an important contribution to halo growth [8].

To compute the total mass growth rate of a halo of a given mass M_0 at time t, we follow the main branch of its merger tree and set $\dot{M} = (M_0 - M_1)/\Delta t$, where M_1 is the mass of this descendant halo's most massive progenitor at time $t - \Delta t$. The mean value of $\dot{M}$ as a function of z for the complete set of resolved haloes in the two Millennium simulations is plotted in Fig. 5 (solid curves). Nine ranges of M_0 spanning five orders of magnitude ($10^{10}\,\mathrm{M}_\odot$ to $10^{15}\,\mathrm{M}_\odot$ from bottom up) are shown. Fig. 5 can be compared directly to Fig. 5 of [9] for the Millennium Simulation alone. The rising $\langle\dot{M}\rangle$ with increasing redshift in our earlier study is seen to continue to $z \sim 14$, and the nearly linear scaling of $\langle\dot{M}\rangle$ with halo mass is extended down to $\sim 10^{10}M_\odot$.

We find the mass accretion rates shown in Fig. 5 to be very well fit by the forms given by equations (8) and (9) of [9]. The coefficients quoted there only need minor adjustments after the Millennium-II results are added. In [10], we proposed the following updated fits to the mean and median mass growth rates of haloes of mass M at redshift z:

$$\langle \dot{M} \rangle = 46.1\ \mathrm{M}_\odot \mathrm{yr}^{-1} \left(\frac{M}{10^{12}\,\mathrm{M}_\odot} \right)^{1.1} (1+1.11z) \sqrt{\Omega_m (1+z)^3 + \Omega_\Lambda} \tag{4.1}$$

and

$$\langle \dot{M} \rangle_{\mathrm{median}} = 25.3\ \mathrm{M}_\odot \mathrm{yr}^{-1} \left(\frac{M}{10^{12}\,\mathrm{M}_\odot} \right)^{1.1} (1+1.65z) \sqrt{\Omega_m (1+z)^3 + \Omega_\Lambda}\,. \tag{4.2}$$

At a given mass and redshift, the mean rate is overall higher than the median rate since the distribution of $\dot{M}$ has a long positive tail. The dashed curves in Fig. 5 illustrate the remarkable accuracy of this formula in matching the simulation results over the broad ranges of halo mass and redshift shown.

5. Summary

The two Millennium simulations, each with ≈ 10 billion particles, have provided us with an unprecedentedly rich database to investigate and quantify the evolution of cosmic structures, the theme of this workshop. These large cosmological simulations are an indispensable tool for following the late-time, nonlinear growth of dark matter haloes.

In this talk, I have presented recent results from the Millennium simulations for the mean merger rates and mass growth history of dark matter haloes as a function of halo mass and redshift. These quantities have not been determined reliably until recently because to do so, one must follow the ancestral relations of haloes backwards in time over many simulation outputs, and quantify the intrinsically multiple-body problem. Only very large simulations such as the Millennium offer sufficient dynamic range for determining these statistics reliably. This feature is unlike many other well-studied properties of haloes, e.g. the mass function, density profiles, shapes, and spins, which do not require merger trees and can therefore be determined from a single simulation output.

I have shown that the merger rate and mass accretion rate of dark matter haloes follow simply mass and time dependence that can be accurately parameterized by fitting formulas given by equations (2.1), (4.1), and (4.2). For the mean merger rate per halo (in units of per redshift), it is nearly independent of z out to $z \sim 15$; the dependence on halo mass is weak ($\propto M_0^{0.13}$); and it is nearly a power law in the progenitor mass ratio ($\propto \xi^{-2}$). For the mass growth rate (in dark matter), the mean and median values are 46 and $25 M_\odot$ yr^{-1} for $10^{12} M_\odot$ haloes at $z = 0$, and the rate increases with mass as $\propto M^{1.1}$ and with redshift as $(1+z)^{2.5}$ (for $z > 1$).

When the haloes are further analyzed as a function of the environment they reside in, we have discovered a *positive* correlation between the merger rate and the local density. This environmental dependence is well approximated by equation (3.4).

Acknowledgments

I wish to thank Dominik Schwarz and Aravind Natarajan for the invitation to attend this interesting workshop, and Gudrun Eickmeyer for help with all the logistics. The work reported in

this talk was mainly carried out by members of my research group, Onsi Fakhouri, Mike Boylan-Kolchin, and James McBride. The Millennium Simulation databases used in this work and the web application providing online access to them were constructed as part of the activities of the German Astrophysical Virtual Observatory.

References

[1] V. Springel et al. (2005), Nature, 435, 629

[2] M. Boylan-Kolchin, V. Springel, S.D.M. White, A. Jenkins, and G. Lemson (2009) MNRAS, 398, 1150

[3] V. Springel, N. Yoshida, S. D. M. White (2001), New Astronomy, 6, 79

[4] V. Springel (2005), MNRAS, 364, 1105

[5] V. Springel, S. D. M. White, G. Tormen and G. Kauffmann (2005), MNRAS, 328, 726

[6] O. Fakhouri and C.-P. Ma (2008), MNRAS, 386, 577

[7] O. Fakhouri and C.-P. Ma (2009), MNRAS, 394, 1825

[8] O. Fakhouri and C.-P. Ma (2010), MNRAS, 401, 2245

[9] J. McBride, O. Fakhouri and C.-P. Ma (2009), MNRAS, 398, 1858

[10] O. Fakhouri, C.-P. Ma and M. Boylan-Kolchin (2010), arXiv:1001.2304